Pure appl. geophys. 158 (2001) 1189–1206
0033–4553/01/071189–18 $ 1.50 + 0.20/0

Pure and Applied Geophysics

Application of Regional Phase Amplitude Tomography to Seismic Verification

W. S. PHILLIPS,[1] H. E. HARTSE,[1] S. R. TAYLOR,[1] A. A. VELASCO[1] and G. E. RANDALL[1]

Abstract—We have applied tomographic techniques to amplitude data to quantify regional phase path effects for use in source discrimination studies. Tomography complements interpolation (kriging) methods by extending our ability to apply path corrections into regions devoid of calibration events, as well as raising levels of confidence in the corrections because of their more physical basis. Our tomography technique solves for resolvable combinations of attenuation, source-generation, site and spreading terms. First difference regularization is used to remove singularities and reduce noise effects.

In initial tests the technique was applied to a data set of 1488, 1.0 Hz, P_g/L_g amplitude ratios from 13 stations for paths inside a 30° by 40° box covering western China and surrounding regions. Tomography reduced variance 60%, relative to the power-law distance correction traditionally applied to amplitude ratios. Relative P_g/L_g attenuation varied with geologic region, with low values in Tibet, intermediate values in basins and high values for platforms and older crust. Spatial patterns were consistent with previous path effect studies in Asia, especially local earthquake coda-Q. Relative spreading was consistent with expected values for P_g and L_g. Relative site terms were similar to one another, yet some tradeoff with attenuation was evident.

Tomography residuals followed systematic trends with distance, which may result from the evolution from direct to coda phases, focusing, model tradeoff or data windowing effects. Examination of the residuals using a kriging interpolator showed coherent geographical variations, indicating unmodeled path effects. The residual patterns often follow geological boundaries, which could result from attenuating zones or minor blockages that are too thin to be resolved, or that have anisotropic effect on regional phases. These results will guide efforts to reparameterize tomography models to more effectively represent regional wave attenuation and blockage. The interpolated residuals also can be combined with predictions of the tomographic model to account for path effects in discrimination studies on a station by station basis.

Key words: Discrimination, tomography, path correction, L_g blockage.

Introduction

Removing the effects of propagation path on seismic amplitudes allows us to isolate source signatures, which should lead to more effective discrimination between natural and man-made events. The Comprehensive Nuclear-Test-Ban Treaty (CTBT) requires us to monitor small events, which increases the importance of

[1] Seismic Research Center, Los Alamos National Laboratory, Los Alamos, New Mexico 87545, USA. E-mail: wsp@lanl.gov

recordings collected at regional distances. Path variations are strong at regional distances because ray paths sample the heterogeneous crust and upper mantle. Thus quantification of regional path effects is a crucial effort for extending Test Ban monitoring techniques to small events.

Path effects include intrinsic attenuation of different crust and upper mantle media, scattering or blockage by structural discontinuities, lateral refraction and multipathing. Seismograms from Tibet and from the Baikal rift, recorded at Lanzhou (LZH) in central China demonstrate the effects different paths can produce on phase amplitudes in a tectonically complex region (Fig. 1). Note the large and impulsive L_g phase from the Baikal event, compared to the lack of L_g from the Tibet event, relative to the P phases. Such behavior has been well documented in China and surrounding regions (e.g., RUZAIKIN *et al.*, 1977; MCNAMARA *et al.*, 1996; RAPINE *et al.*, 1997).

Our strategy is to predict path effects on earthquake data by whatever means, and use this information to improve event identification and magnitude estimates on a station by station basis. To facilitate the event identification, corrections are expected to reduce the scatter in the earthquake population of discriminant ratios such as P_g/L_g (e.g., TAYLOR *et al.*, 1989). In addition, the corrections eliminate the effect of path on any separation between earthquake and explosion populations, and may act to increase or decrease that separation. Decreasing the separation is not necessarily detrimental; otherwise, we employ a practice of identifying events based on their path effects, which in many cases, is just a complicated way to discriminate based on event

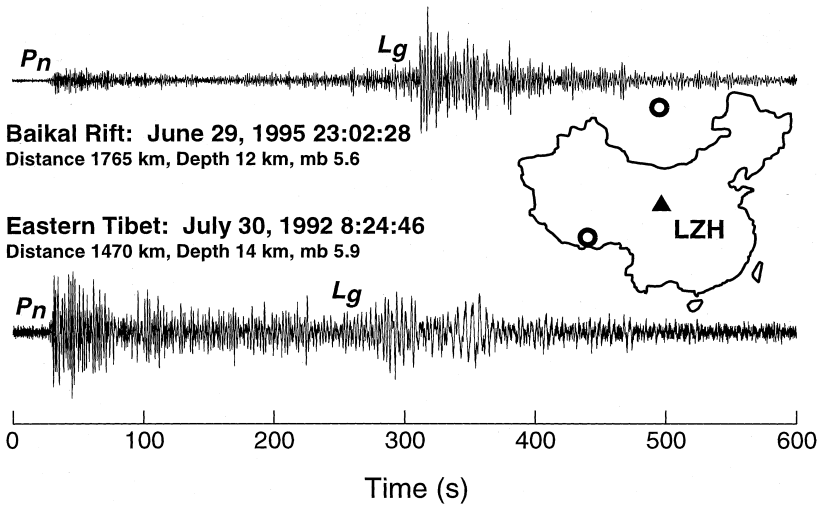

Figure 1

Sample, vertical component, broadband seismograms from the Baikal rift (top) and from eastern Tibet (bottom), recorded at LZH. The seismograms have been high-pass filtered at 0.5 Hz and aligned on their P_n arrival times. The L_g arrival is marked at its expected position in the Tibetan event record. Event (circles) and station (triangle) locations are indicated on the map.

epicenter. However, because we use only earthquakes to predict path effects, shallow path effects, or free-surface effects such as R_g to L_g scattering are largely ignored. Thus, after path correction, the discriminant ratio for an explosion or an exceptionally shallow earthquake will retain the shallow path or near-surface effect and may stand out on a discrimination plot for that reason. This depth effect is desirable if and when it occurs, because depth is an effective discriminant and depths are not generally well known for crustal sources.

Interpolation has been shown to be an effective path correction method, in terms of reducing variance in amplitude data (TAYLOR and HARTSE, 1998; PHILLIPS *et al.*, 1998; PHILLIPS, 1999; RODGERS *et al.*, 1999). These studies demonstrate that interpolated regional phase amplitude surfaces correlate well with regional geology, especially at lower frequencies (1 Hz); thus the results reflect path, rather than coherent source radiation or depth effects. Although earlier work was performed with simple, moving window smoothers, the non-stationary Bayesian kriging interpolator described by SCHULTZ *et al.* (1998) is more appropriate for monitoring work. Kriging provides error estimates and continuously differentiable surfaces, while the Bayesian modifications control extrapolation of the surface and errors into regions devoid of calibration events. In particular, the interpolated values go to zero and the interpolated errors go to the specified background error in such regions. This allows the inclusion of detailed background models by kriging the model residuals and merging the results with a map of the model predictions and errors. Background models provide the ability to extrapolate with added confidence and are the focus of this study. The resulting surface can be used as a lookup table to quickly correct for path effects during routine monitoring.

Another effective path correction method that has been tested extensively is the waveguide or path-parameter method. This method relies on correlations of amplitude data with readily available physical data such as topography, basin thickness or Moho depth to predict path effects (e.g., ZHANG and LAY, 1994; FAN and LAY, 1998; HARTSE *et al.*, 1998). The idea behind this method is that even though the topography, to choose one, may not be the physical cause of the path-effect variations, it may be correlated with the phenomena that are responsible. For example, elevated or rough topography could correlate with high intrinsic attenuation, both characteristic of an active tectonic region. The waveguide method is less effective than interpolation in reducing variance in amplitude data (PHILLIPS, 1999; RODGERS *et al.*, 1999), but is better able to predict data where no calibration events exist. PHILLIPS (1999) demonstrated the use of a waveguide model as a background model by applying Bayesian kriging interpolation to the waveguide model residuals; yielding a correction surface that matched data well in active regions and extrapolated more effectively into inactive regions.

Tomographic images of the attenuation of regional phases and coda can also be used to predict path effects (e.g., SINGH and HERRMANN, 1988; CAMPILLO, 1987; XIE and MITCHELL, 1990; CAMPILLO *et al.*, 1993; MITCHELL *et al.*, 1997; SANDVOL *et al.*,

1998). Tomography complements interpolation methods because images can be well resolved in areas where no calibration events occur. In addition, the physical basis of tomography increases our confidence in the derived path corrections. In this study we test tomography techniques using regional phase amplitude-ratio data, with emphasis on employing results as a background model, with or without additional kriged corrections, for use in an automatic monitoring scheme.

In initial tests we applied tomography techniques to 1 Hz P_g/L_g amplitude-ratio data. The use of ratio data decreases the influence of a possibly error prone, teleseismically determined m_b that is used to correct for source size and scaling prior to inversion. Of course, using ratios will lead to difficulties in interpreting results because two phases are involved. In addition, monitoring would require a correction surface for every ratio that might be desired, which is a large number if we consider all bands and phases that can be observed. For these reasons we support the use of single-phase correction surfaces for routine monitoring and plan to test the applicability of single-phase tomography to monitoring in future work.

The 1-Hz band we have chosen is useful for technique development in that it offers the most data and coverage. The 1-Hz ratios can improve the performance of multivariate discriminants (TAYLOR and HARTSE, 1997); however they generally perform poorly on their own (WALTER *et al.*, 1995; TAYLOR, 1996; HARTSE *et al.*, 1997). Results in this band can still be useful for magnitude estimation or for defining geophysically distinct regions that will be beneficial for assessing the progress of calibration efforts. As we move to higher frequencies, our hope is that path corrections will lower the frequency threshold at which source types are observed to separate (3–4 Hz), allowing the inclusion of smaller and more distant events that might be of poor signal-to-noise in the most effective discriminant bands (6–8 Hz).

Below we will outline data reduction procedures for stations in China and surrounding regions, and describe the tomographic method we applied. We will show relative attenuation results that correlate well with geological province as well as spatially coherent, unmodeled data that suggest new avenues of development.

Data

We used the Preliminary Determination of Epicenters catalog to guide the collection of regional earthquake data, archived at the Incorporated Research Institutions for Seismology, Data Management Center. For this study, we used data from earthquakes occurring between 1986 and 1996 recorded by 13 stations from China and surrounding areas: Enshi (ENH), Lhasa (LSA), Lanzhou (LZH), Urumchi (WMQ) and Xian (XAN) in China; as well as Boravoye (BRVK), Kurchatov (KURK) and Makanchi (MAK), Kazakhstan; Ala-Archa (AAK), Kirghizstan; Talaya (TLY) and Zalesovo (ZAL), Russia; Nilore (NIL) Pakistan; and Ulan Bator (ULN), Mongolia.

To process the data we first determined arrival times of the regional phases manually. After correcting for the instrument, RMS amplitudes were obtained for a number of pass bands between 0.5 and 8 Hz, using time-domain filtering techniques, aligning windows on picked arrivals if they existed or on preset group velocities if arrivals were not picked (HARTSE *et al.*, 1997). We used vertical component P_g/L_g ratios in the band 0.75 to 1.5 Hz in this study. The preset L_g group-velocity window was 3.6 to 3.0 km/s and the P_g group-velocity window was 6.2 to 5.2 km/s. Requiring paths to lie within a box defined by longitudes 70° to 110° and latitudes 25° to 55°, as well as distances between 300 and 2500 km, event depths less than 50 km and signal-to-noise (pre-*Pn*) greater than 2 for both phases, reduced the data set to 1488 measurements. A plot of the ray-path distribution indicates good coverage over most of the region (Fig. 2).

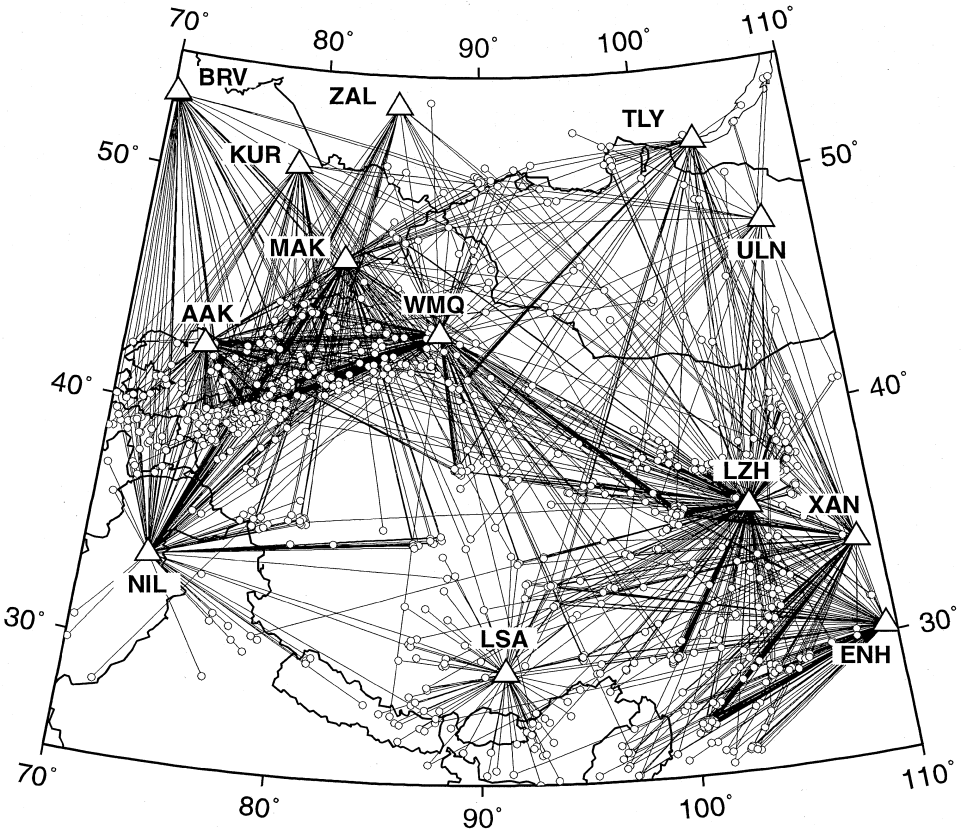

Figure 2
Great-circle ray paths representing data used in tomographic inversion. Stations are indicated by triangles and events by circles.

Tomography Method

Using tomographic techniques we solve for resolvable combinations of relative attenuation, site and spreading effects on regional phase amplitudes or amplitude ratios. For a homogeneous velocity model we express amplitude for a given frequency band,

$$a_{ijk} = c_k f(m_b^i) s_{jk} x_{ij}^{-\beta_k} \mathrm{e}^{-\alpha_k x_{ij}} \quad ,$$

where the i, j, k indices represent source, site and phase type, respectively, c_k is a source generation term, f is source scaling, taken as a known function of m_b and frequency (CONG *et al.*, 1996; equations (6) and (10)), s_{jk} is site effect, x_{ij} is distance, β_k is the spreading coefficient and α_k is the spatial attenuation coefficient. We define a source-corrected amplitude,

$$d_{ijk} = a_{ijk} / f(m_b^i) \quad .$$

Taking logarithms,

$$\log_{10} d_{ijk} = \log_{10} c_k + \log_{10} s_{jk} - \beta_k \log_{10} x_{ij} - \alpha_k x_{ij} \log_{10} \mathrm{e} \quad .$$

Substituting capitals for $\log_{10}$ yields,

$$D_{ijk} = C_k + S_{jk} - \beta_k X_{ij} - \alpha_k x_{ij} \log_{10} \mathrm{e} \quad .$$

We now discretize attenuation into an array of evenly spaced, latitude–longitude centered ellipses of constant α_k, setting major and minor axes to $\sqrt{2/2}$ of the local grid spacing so ellipses centered on a box of four adjacent grid points meet at a single point in the center (Fig. 3). Assuming a great-circle path, we take the chord length across each ellipse it intersects and normalize such that the sum of normalized chords becomes the total path length in degrees. Thus $\alpha_k x_{ij}$ becomes a sum of products of discretized α_k and normalized ellipse chords,

$$D_{ijk} = C_k + S_{jk} - \beta_k X_{ij} - \log_{10} \mathrm{e} \sum_m \alpha_{km} \delta x_{ijm} \quad , \tag{1}$$

where the new index, m, represents the discretization of the attenuation model and the δx_{ijm} are the normalized ellipse-chord lengths. After taking phase ratios, relative generation, site, spreading and attenuation terms replace those of equation (1) (dropping the phase index, k),

$$\Delta D_{ij} = \Delta C + \Delta S_j - \Delta\beta X_{ij} - \log_{10} \mathrm{e} \sum_m \Delta\alpha_m \delta x_{ijm} \quad . \tag{2}$$

This relies on our homogeneous model assumption that requires both rays to take the same, great-circle path. Note that the effect of the source-scaling corrections, $f(m_b^i)$, cancel or are reduced, depending on the frequency bands and event size. Tomographic inversion can be based on these linear equations once we rationalize singularities or tradeoffs between unknown parameters.

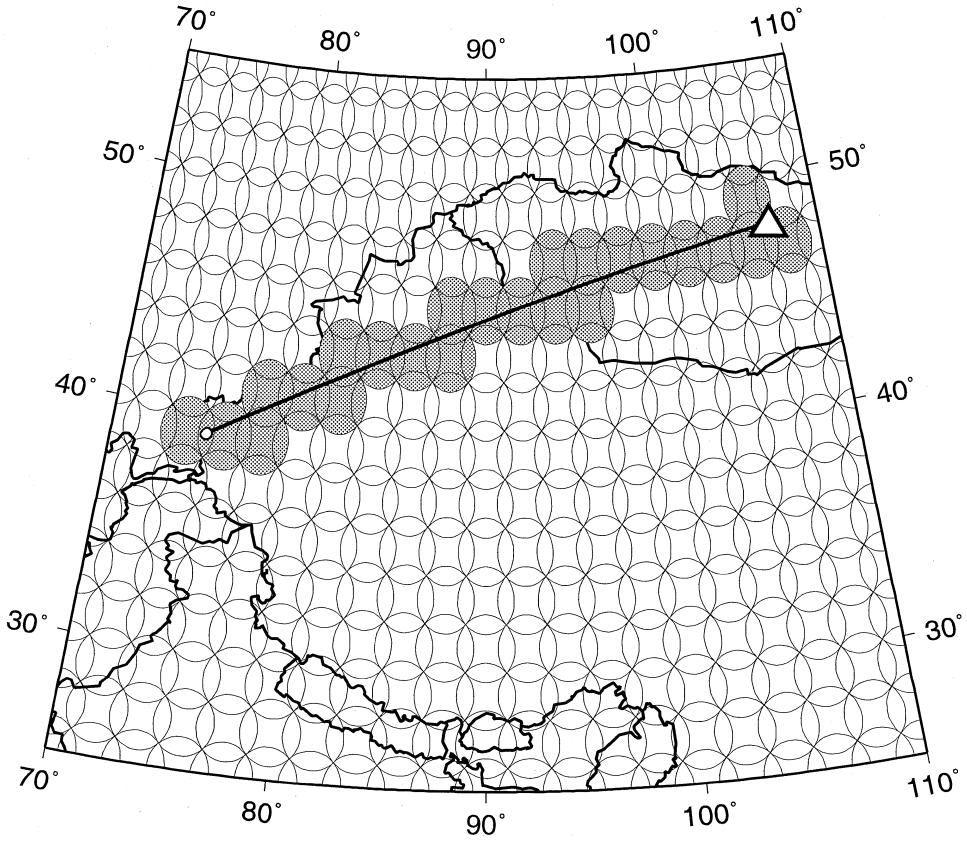

Figure 3
Array of ellipses used to parameterize attenuation. A 2° spacing is shown.

We use standard, least-squares techniques to solve equations (1) or (2), which can be written in matrix form,

$$\mathbf{Ax} = \mathbf{d} \ ,$$

where **d** is the data vector, **x** is the vector of unknowns and **A** represents the model equations. We apply first difference regularization to reduce the influence of noise on the results and to eliminate singularities due to unresolved combinations of model parameters. First difference regularization adds equations that constrain adjacent model parameters (in the case of attenuation terms) to be similar, weighted by a regularization parameter, which balances the importance of the constraint relative to constraints provided by the data. The larger the regularization parameter, the smoother the resulting image. Second difference regularization is often used in tomographic studies, although the first difference is more powerful in resolving singularities (e.g., PHILLIPS and FEHLER, 1991). The least-squares solution is written

$$\mathbf{x} = (\mathbf{A}^t\mathbf{W}^t\mathbf{W}\mathbf{A} + \mathbf{S}^t\Lambda^2\mathbf{S})^{-1}\mathbf{A}^t\mathbf{W}^t\mathbf{d} \ , \tag{3}$$

where $\mathbf{S}$ represents the regularization equations, constraining certain model parameters to be similar, $\mathbf{\Lambda}$ is a diagonal matrix containing regularization weights, $\mathbf{W}$ is a diagonal matrix representing weights based on estimated data error and superscript t represents the transpose. In practice, we use one regularization weight for attenuation terms (λ_α) and another for site terms (λ_s). In addition, we assume data error to be uniform. Resolution and covariance are calculated via

$$\mathbf{R} = (\mathbf{A}^t\mathbf{W}^t\mathbf{W}\mathbf{A} + \mathbf{S}^t\Lambda^2\mathbf{S})^{-1}\mathbf{A}^t\mathbf{W}^t\mathbf{W}\mathbf{A},$$
$$\mathbf{C} = (\mathbf{A}^t\mathbf{W}^t\mathbf{W}\mathbf{A} + \mathbf{S}^t\Lambda^2\mathbf{S})^{-1} \ .$$

We can also estimate the variance of the predicted value along a new path,

$$\boldsymbol{\sigma}_p^2 = \mathbf{a}^t\mathbf{C}\mathbf{a} \ ,$$

where $\mathbf{a}$ is a column vector representing equation (1) or (2) for that path, similar to a row of $\mathbf{A}$ (e.g., DRAPER and SMITH, 1981). This will provide errors for the amplitude correction surface generated from the tomographic image. In addition, the prediction error can be included when applying Bayesian kriging to tomography residuals, if we wish to combine tomography and interpolation results into one correction surface. The prediction error may also be useful for combining predictions of different background models, such as waveguide and tomography models, into one correction surface.

The tomographic calculations have been implemented using a Jacobi conjugate gradient solver (ITPACK). Coarse grid calculations were confirmed with a standard L-U decomposition code. We added switches that eliminate or combine unknown terms in equations (1) and (2) to avoid singularities. For example, the generation term (ΔC) must be combined with the site terms (ΔS_j) because neither can be resolved uniquely. More subtle tradeoffs can be evaluated by examining the resolution matrix.

We use residual variance to evaluate goodness of fit and model improvement. The trace of the resolution matrix is taken as the number of free parameters in the model (TARANTOLA, 1987), which is needed to calculate variance. Variance reduction will be quoted relative to a power-law fit with distance, which is the traditional correction for amplitude ratios in discrimination studies (e.g., HARTSE *et al.*, 1997).

Results

To parameterize the inversion we examined residual variance for a range of discretization intervals and regularization parameters. For this study, 1° and 2° attenuation term grids allowed similar fits to data, while a 5° grid was too coarse to fit the data well (Fig. 4). Results employing a grid spacing of 2° will be presented

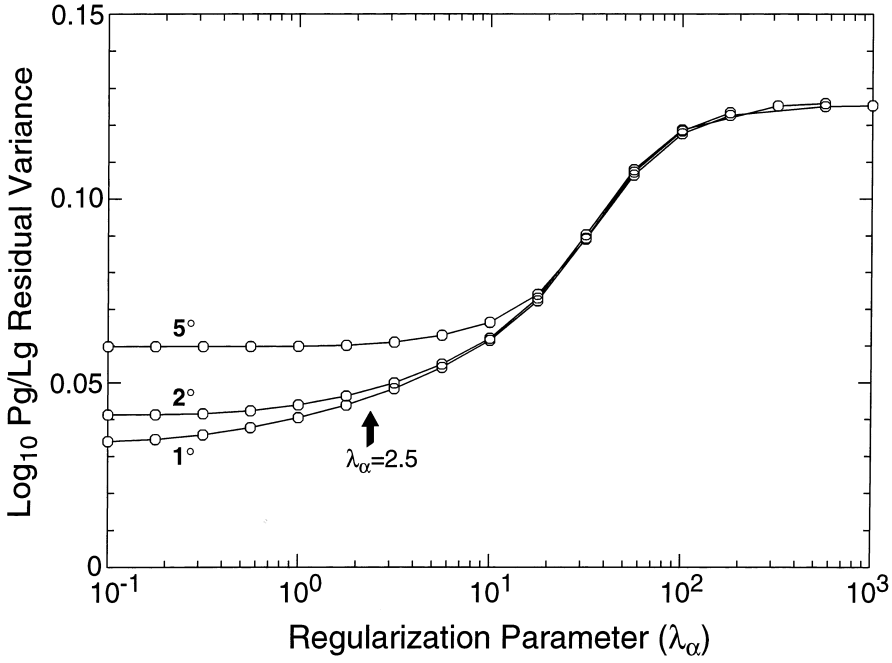

Figure 4
$\mathrm{Log}_{10} P_g/L_g$ residual variance versus attenuation regularization parameter. Results for 1°, 2° and 5° grid spacings are shown as marked. A regularization parameter of 2.5 was used in this study.

here. Regularization parameters must be chosen large enough to control the effects of noise, yet lie below the point where excessive smoothing causes the residual variance to increase rapidly (e.g., PHILLIPS and FEHLER, 1991). Our choice of 2.5 for attenuation regularization (Fig. 4) allowed 58 free parameters in the 2° model, as estimated from the trace of the attenuation portion of the resolution matrix. This number of free parameters is similar to that obtainable with an unregularized 5° grid; however the finer grid allows more spatial freedom to fit the data. Holding attenuation regularization fixed, the site term regularization parameter was determined to be 0.5, following the same procedure. This regularization constrains poorly resolved site terms to be similar to well resolved site terms and helps to avoid tradeoffs between site and near-station attenuation terms.

After removing a power-law fit with distance, we found the standard deviation of the residuals to be 0.36, representing the initial scatter in the ratio data. Allowing attenuation, spreading and source generation terms free produced a residual standard deviation of 0.23, or a variance reduction of 59% relative to the power-law fit. Replacing the source generation term with individual site terms resulted in only slight improvement and a variance reduction just over 60%. We plot relative P_g/L_g attenuation, $\Delta\alpha_m$, in color (Fig. 5). As the equations are set up, positive $\Delta\alpha_m$

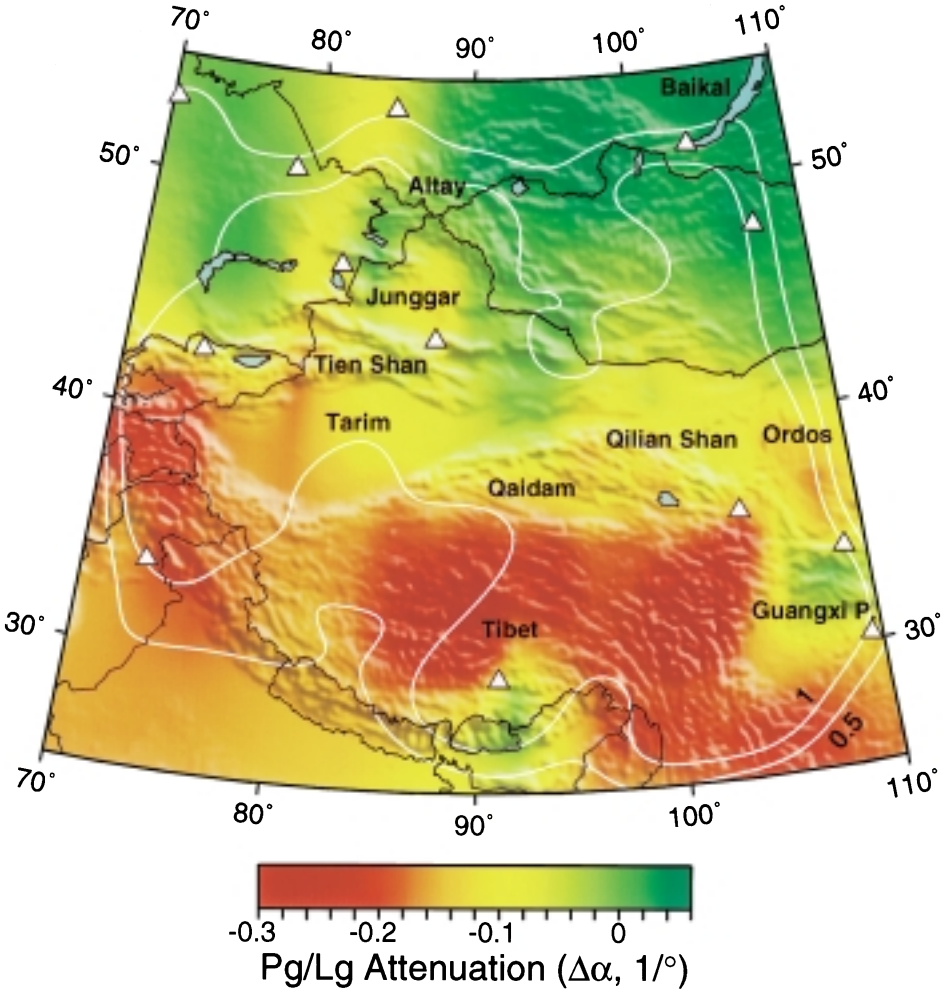

Figure 5
Relative attenuation from tomographic inversion of 1 Hz, P_g/L_g ratios. Green represents high relative attenuation (P_g attenuation high; L_g, low); red, *vice versa*. Colors are superposed on a topography gradient map. White contours indicate resolution as discussed in the text. Annotations mark geographical and geological features mentioned in the text. Triangles represent stations that provided data for this study.

(green) indicate P_g attenuates faster than L_g, while negative $\Delta\alpha_m$ (red) indicate the opposite. The tomography results are superposed on a topography map for interpretation purposes. Well-resolved portions of the image are indicated by contours of the diagonal component of the resolution, normalized by the ratio of the number of grid points to free parameters in the attenuation model. The normalization adjusts for regularization effects, which reduce resolution by averaging adjacent model parameters.

We found that P_g/L_g attenuation correlates well with geological province. The lowest values (low P_g, high L_g attenuation) fall within the Tibetan Plateau. This low is bounded sharply to the north by the Qaidam Basin, and to the east by the Guangxi platform. Intermediate to low values can be seen in the Qilian Shan and western Tian Shan ranges, as well as the Tarim, Ordos and Junggar Basins. Note the sharp transition between the Junggar Basin area and the surrounding mountain ranges. High P_g/L_g attenuation is found in the stable platform areas to the north and in the Guangxi platform to the east. Higher values are also found for trans-Himalaya paths to Lhasa (LSA), similar to patterns noted in spectral Q studies of regional phases recorded at LSA (REESE *et al.*, 1998). We expected higher values in the vicinity of station ZAL in Russia; however, the weak L_g observed for paths through the Tian Shan and border ranges, relative to other paths through the northern area, is responsible for the low pattern.

Relative site terms ranged from −0.8 to −0.3 for these data (Fig. 6), most clustering about −0.5. The mean can be considered the relative source generation term, which is incorporated into the site terms in this inversion. Including these terms improves the fit to data only slightly, yet adds definition to the attenuation image as site effects are more appropriately accounted for. The similarity between most well resolved, site terms may be an advantage of applying tomography to ratio data. However, two outlier site terms (KURK and LSA) appear to reflect the attenuation from nearby areas, even though these terms are reasonably well resolved.

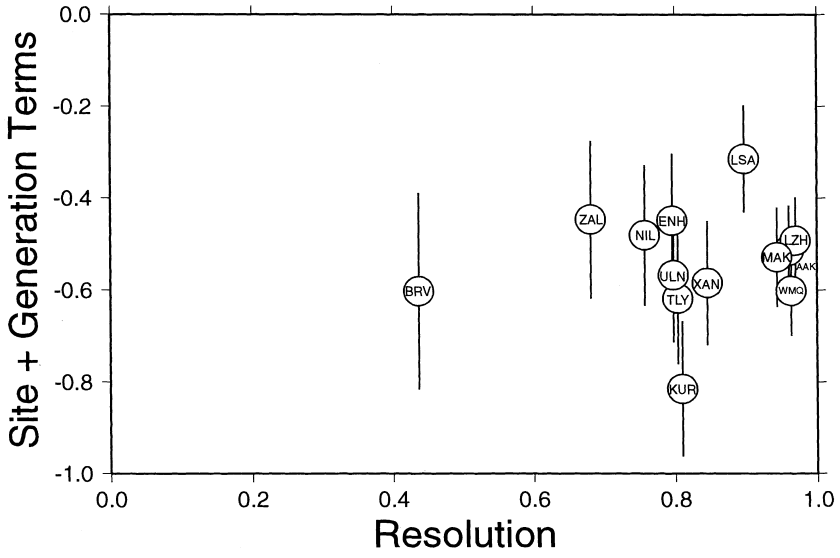

Figure 6
Relative site terms versus their resolution. Station names are indicated. Error bars represent twice the standard error of the estimate.

The relative spreading coefficient, $\Delta\beta$, was estimated to be 0.54 ± 0.11 (standard error). Again, the positive value indicates P_g spreads more quickly than L_g. Synthetic calculations generated using the inversion result and including similar levels of Gaussian noise resulted in correct recovery of the results, with some tradeoff evident between spreading and the range of attenuation terms. Based on 100 runs with different realizations of noise, the mean and standard deviation of the recovered $\Delta\beta$ was 0.50 ± 0.08.

Discussion

The tomography image is similar to results from previous Eurasian path effect studies. If we interpret the variation of P_g/L_g attenuation primarily to be the result of L_g effects (PHILLIPS *et al.*, 1998), we can compare with studies of L_g and L_g coda. RAPINE *et al.* (1997) prepared a qualitative map of L_g propagation in China, based on regional data from many stations. Most of China is described as efficient for L_g, while the Tibetan Plateau is described as inefficient. The boundary between the propagation regions matches our tomographic result reasonably well. We fail to see an attenuating zone for L_g along the Tibetan Plateau edges, as suggested by MCNAMARA *et al.* (1996); however, our signal-to-noise criteria have omitted most blocked L_g paths from the study and the regularization constraints act to smooth the influence of the few that remain. MITCHELL *et al.* (1997) produced a tomographic map of 1 Hz, L_g coda Q for Eurasia. This map is roughly consistent with ours, except for Mongolia, where we see efficient L_g (high P_g/L_g attenuation) and the L_g coda Q predicts inefficient L_g. However, the L_g coda-Q maps are of significantly larger scale and lower resolution than those presented here. Perhaps the best correspondence, in terms of spatial resolution, is with results of a local earthquake, crustal coda-Q study (JIN and AKI, 1988). The coda-Q measurements are unevenly distributed through China; however, where coverage is dense, such as along the eastern boundary of the Tibetan Plateau, the patterns are very similar to ours. This points out the value to discrimination research in performing local earthquake coda-Q studies in regions of dense station coverage, with care taken to limit the coda lapse times so only crustal materials are sampled (PHILLIPS *et al.*, 1988).

The distribution of data that are inconsistent with the tomography result can help us understand how well the underlying assumptions have been satisfied. We first examine residuals (data minus prediction) as a function of source–receiver distance by taking means within equally spaced bins in the logarithmic domain (Fig. 7). Recall that the relative spreading coefficient, $\Delta\beta$, was determined to be 0.54 ± 0.11 in our inversion. This indicates that P_g spreads faster than L_g so that ratios decrease with distance. In this discussion we refer to spreading loosely, intending apparent spreading, including possible measurement effects rather than pure geometrical spreading. Our $\Delta\beta$ of 0.54 can be thought to correspond to the zero-residual line in

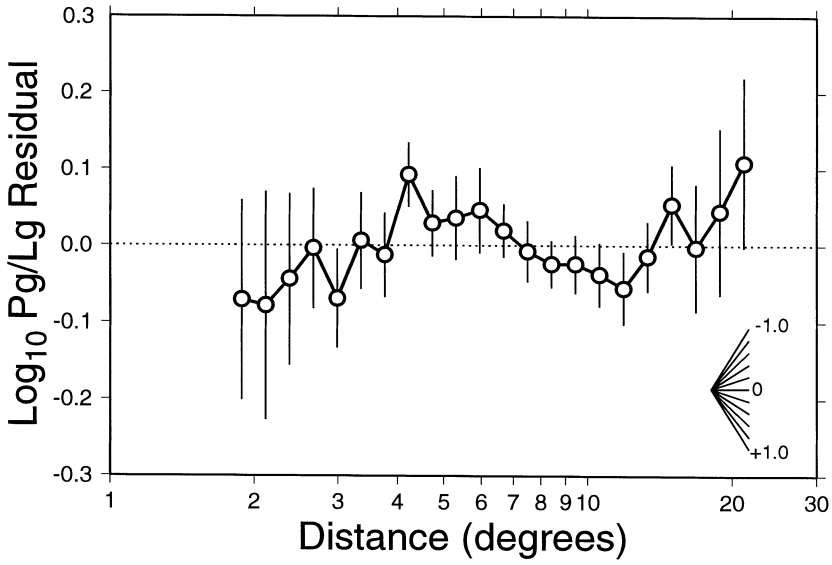

Figure 7
$\mathrm{Log}_{10} P_g/L_g$ residuals (data minus prediction) binned by distance. Error bars represent twice the standard error of the mean. Spreading values relative to zero slope are indicated in the lower right corner.

Figure 7. We observe three ranges of similar trend in the residuals: up to 500 km, where spreading is 0.3 less than $\Delta\beta$; 500 to 1200 km, where spreading is 0.3 greater than $\Delta\beta$; and beyond 1200 km, where spreading is 0.4 less than $\Delta\beta$. Note the slopes read off the plot are opposite in sign to the change in spreading value because of the sign conventions in the inversion equations. Error bars show the middle trend is the most significant. These trends can result from a number of factors including: evolution from direct to coda energy; focusing of mantle P affecting P coda, thus P_g; tradeoffs with attenuation; and window-length, measurement effects. We further note that residuals are low for short distances and high for long distances, implying an underestimation of $\Delta\beta$ due to the influence of data from the extremes on the fitting. If we assume L_g spreading is 0.83 (NUTTLI, 1973; CAMPILLO *et al.*, 1984), our $\Delta\beta$ of 0.54 or greater implies a P_g spreading coefficient of 1.37 or greater, reasonably consistent with a numerical modeling estimate of 1.5 (CAMPILLO *et al.*, 1984). Clearly, further effort is warranted to understand distance trends in these data. Evaluation of various effects may be easier when single-phase data are inverted rather than ratios.

To examine the geographical distribution of inconsistent data we interpolate tomography residuals, one station at a time. Interpolation is performed with a Bayesian kriging algorithm (SCHULTZ *et al.*, 1998), using a data correlation function appropriate for L_g amplitudes in central China (ANDERSON and PHILLIPS, 1998). For all stations we see coherent geographical variations, indicating path effects that are inconsistent with the tomography result. For many stations, such as BRVK (Fig. 8),

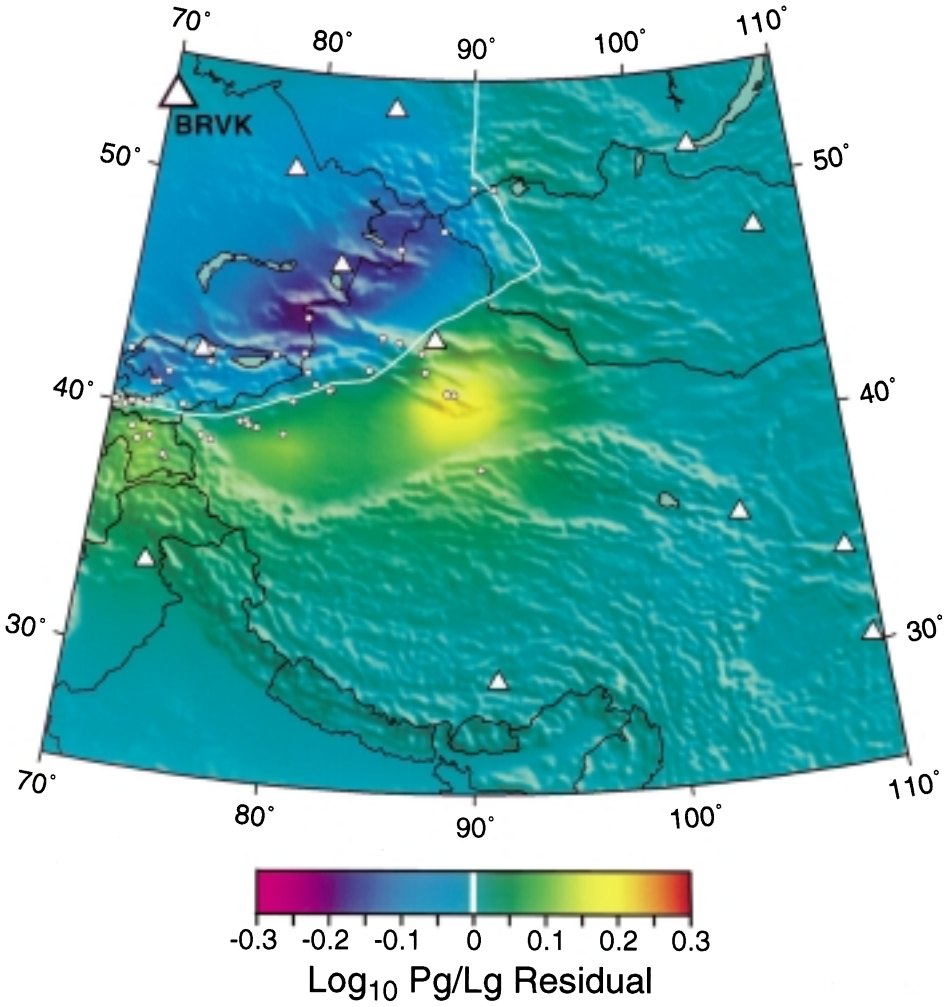

Figure 8
Spatial interpolation of $\log_{10} P_g/L_g$ residuals (data minus prediction) from station BRVK obtained by kriging. Warm colors represent underprediction, cold colors overprediction. Underpredicted data seek lower relative attenuation (warmer colors) along their paths through the tomography image (Fig. 5), overpredicted data, the opposite. Colors are superposed on a topography gradient map. A white line represents the zero contour. Triangles represent stations and small circles show locations of events recorded at BRVK that provided useable data to the study.

we see residual patterns that follow boundaries between geological regions. For BRVK a sudden increase in P_g/L_g ratios south of the Tian Shan may indicate a long, thin zone of high L_g attenuation, or a blockage. The high attenuation may be a structural or scattering, rather than an intrinsic, effect (e.g., BAUMGARDT, 1990). The blockage may have greater effect on ray paths traveling across the structure (to

BRVK, for example) than on ray paths traveling along the structure. Subparallel ray paths would tend to wash out the high attenuation zone during tomographic inversion. Our smoothing and coarse parameterization contribute to this effect.

The inconsistent data patterns suggest future modification of the tomography methods. We can explore the relaxation of regularization constraints in well resolved areas. We can also include anisotropic effects into the model parameterization, as has been done for velocity tomography (HEARN, 1996), and which may help resolve blockages. Lateral refraction and multipathing will also appear as inconsistent data; we may have to rely on numerical modeling to evaluate the importance of these effects.

More general improvement could come from the addition of constraints from censored (poor signal-to-noise) data into the tomography, especially for blocked L_g paths, as well as realistic data covariance reflecting correlation between data from similar paths. Furthermore, better magnitude estimates will reduce noise introduced by source corrections based on teleseismic m_b and facilitate the use of phase amplitude data, rather than ratios. The magnitudes could be improved by accounting for censoring effects on teleseismic amplitudes (e.g., MCLAUGHLIN, 1988), or by using regional envelopes or coda (AKI, 1980; MAYEDA, 1993). Tomography of phase amplitudes, as opposed to ratios, will be simpler to interpret and implement into production schemes. Comparison with ratio tomography results will indicate how well source effects have been accounted for.

The tomographic results can be used to correct for path effects and reduce scatter in discrimination studies. For a grid surrounding each station we can predict amplitudes or amplitude ratios, along with their errors. These surfaces can be used during the course of routine processing. In addition, the tomography can be employed as a background model, and corrections calculated by applying Bayesian kriging to the residuals (Fig. 8) to form the final correction surface. The kriging can allow for the tomography prediction errors in creating the correction surface. The final result will reflect the tomography model in areas where events rarely occur and an interpolated version of the data in areas where events do occur.

Conclusions

We have applied tomographic techniques to regional phase, amplitude-ratio data to solve for resolvable combinations of relative attenuation, source generation, site and spreading effects. The main benefit of using ratio data is the reduced importance of source corrections which introduce noise.

We obtained a variance reduction of 60% for 1488 P_g/L_g ratios in the 0.75–1.5 Hz band for a 30° by 40° box, covering western China and surrounding areas. Relative P_g/L_g attenuation correlated with geological province and compared well with previous studies of L_g, L_g coda and S coda of varying geographical resolution. Regions such as western Tibet were poorly resolved because blocked L_g paths were

excluded from the study; the inclusion of the censored data constraints should improve the final model. Relative spreading was estimated to be 0.54 ± 0.11, consistent with literature values for P_g and L_g spreading. Interpolation of residuals showed coherent spatial patterns, indicating significant amounts of unmodeled path effect. Some unmodeled path variation can be attributed to long, thin zones of high attenuation, or blockage that are smoothed over in the tomographic image. Relaxing regularization constraints in well-resolved regions, and including anisotropy, may allow these zones to be modeled more effectively.

The tomography results can be used to predict correction factors and errors for source discrimination studies. In addition, residuals can be interpolated and added to corrections for a given station to combine the extrapolation power of tomography with the better fit to data of the interpolation methods.

Acknowledgments

Chris Young and Jim Hipp provided the Bayesian kriging code as well as needed guidance. We also thank Dan McNamara and an anonymous reviewer for their suggestions. Seismic data were retrieved from the IRIS DMC, GTOPO30 topography from the USGS. GMT and SAC software were used extensively. This work was performed under the auspices of the US Department of Energy by Los Alamos National Laboratory under Contract W-7405-ENG-36.

References

Aki, K. (1980), *Physical Basis for the Duration Magnitude and Recommended Practice for Coda Magnitude Determination*, Proc. 17th Assemb. ESC, Budapest, 73–77.

Anderson, K. K., and Phillips, W.S. (1998), *A Simple Procedure for Kriging Left-censored Data*, EOS Trans. Am. Geophys. U. *79*, F555.

Baumgardt, D. (1990), *Investigation of Teleseismic L_g Blockage and Scattering Using Regional Arrays*, Bull. Seismol. Soc. Am. *80*, 2261–2281.

Campillo, M., Bouchon, M., and Massinon, B. (1984), *Theoretical Study of the Excitation, Spectral Characteristics and Geometrical Attenuation of Regional Seismic Phases*, Bull. Seismol. Soc. Am. *74*, 79–90.

Campillo, M. (1987), *L_g Wave Propagation in a Laterally Varying Crust and the Distribution of the Apparent Quality Factor in Central France*, J. Geophys. Res. *92*, 12604–12614.

Campillo, M., Feignier, B., Bouchon, M., and Bethoux, N. (1993), *Attenuation of Crustal Waves across the Alpine Range*, J. Geophys. Res. *98*, 1987–1996.

Cong, L. L., Xie, J. K., and Mitchell, B. J. (1996), *Excitation and Propagation of L_g from Earthquakes in Central Asia with Implication for Explosion/Earthquake Discrimination*, J. Geophys. Res. *101*, 27779–27789.

Draper, N. R., and Smith, H., *Applied Regression Analysis*, *Second Edition* (John Wiley & Sons, New York 1981).

Fan, G., and Lay, T. (1998), *Statistical Analysis of Irregular Waveguide Influences on Regional Seismic Discriminants in China*, Bull. Seismol. Soc. Am. *88*, 74–88.

HARTSE, H. E., TAYLOR, S. R., PHILLIPS, W. S., and RANDALL, G. E. (1997), *A Preliminary Study of Regional Seismic Discrimination in Central Asia with Emphasis on Western China*, Bull. Seismol. Soc. Am. *87*, 551–568.

HARTSE, H. E., FLORES, R. A., and JOHNSON, P. A. (1998), *Correcting Regional Seismic Discriminants for Path Effects in Western China*, Bull. Seismol. Soc. Am. *88*, 596–608.

HEARN, T. (1996), *Anisotropic Pn Tomography in the Western United States*, J. Geophys. Res. *101*, 8403–8414.

JIN, A., and AKI, K. (1988), *Spatial and Temporal Correlation between Coda Q and Seismicity in China*, Bull. Seismol. Soc. Am. *78*, 741–769.

MCNAMARA, D. E., OWENS, T. J., and WALTER, W. R. (1996), *Propagation Characteristics of L_g across the Tibetan Plateau*, Bull. Seismol. Soc. Am. *86*, 457–469.

MAYEDA, K. (1993), *$m_{bL_g\text{coda}}$: A Stable Single Station Estimator of Magnitude*, Bull. Seismol. Soc. Am. *83*, 851–861.

MCLAUGHLIN, K. L. (1988), *Maximum-likelihood Event Magnitude Estimation with Bootstrapping for Uncertainty Estimation*, Bull. Seismol. Soc. Am. *76*, 855–862.

MITCHELL, B. J., PAN, Y., XIE, J., and CONG, L. (1997), *L_g Coda Q Variation across Eurasia and its Relation to Crustal Evolution*, J. Geophys. Res. *102*, 22,767–22,779.

NUTTLI, O. W. (1973), *Seismic Wave Attenuation and Magnitude Relations for Eastern North America*, J. Geophys. Res. *78*, 876–855.

PHILLIPS, W. S., LEE, W. H. K., and NEWBERRY, J. T. (1988), *Spatial Variation of Crustal Coda Q in California*, Pure appl. geophys. *128*, 251–260.

PHILLIPS, W. S., and FEHLER, M. C. (1991), *Traveltime Tomography: A Comparison of Popular Methods*, Geophysics *56*, 1639–1649.

PHILLIPS, W. S., RANDALL, G. E., and TAYLOR, S. R. (1998), *Path Correction Using Interpolated Amplitude Residuals: An Example from Central China*, Geophys. Res. Lett. *25*, 2729–2732.

PHILLIPS, W. S. (1999), *Empirical Path Corrections for Regional Phase Amplitudes*, Bull. Seismol. Soc. Am. *89*, 384–393.

RAPINE, R. R., NI, J. F., and HEARN, T. M. (1997), *Regional Wave Propagation in China and its Surrounding Regions*, Bull Seismol. Soc. Am. *87*, 1622–1636.

REESE, C. C., RAPINE, R. R., and NI, J. F. (1998), *Lateral Variation of P_n and L_g Attenuation at the CDSN Station LSA*, Bull. Seismol. Soc. Am. *88*, 325–330.

RODGERS, A. J., WALTER, W. R., SCHULTZ, C., MYERS, S., and LAY, T. (1999), *A Comparison of Methodologies for Representing Path Effects on Regional P/S Discriminants*, Bull. Seismol. Soc. Am. *89*, 394–408.

RUZAIKIN, A. I., NERSESOV, I. L., KHALTURIN, V. I., and MOLNAR, P. (1977), *Propagation of L_g and Lateral Variations in Crustal Structure in Asia*, J. Geophys. Res. *82*, 307–316.

SANDVOL, E., SEBER, D., BARAZANGI, M., MOHAMAD, R., TURKELLI, N., GURBUZ, C., ZOR, E., and GOK, R. (1998), *Seismological Research in the Middle East*, Proceedings, 20th Ann. Seis. Res. Symp. Santa Fe, 745–753.

SCHULTZ, C., MYERS, S., HIPP, J., and YOUNG, C. (1998), *Nonstationary Bayesian Kriging: Application of Spatial Corrections to Improve Seismic Detection, Location and Identification*, Bull. Seismol. Soc. Am. *88*, 1275–1288.

SINGH, S., and HERRMANN, R. B. (1988), *Regionalization of Crustal Coda-Q in the Continental United States*, J. Geophys. Res. *88*, 527–538.

TARANTOLA, A. *Inverse Problem Theory* (Elsevier, Amsterdam 1987).

TAYLOR, S. R., DENNY, M. D., VERGINO, E. S., and GLASER, R. E. (1989), *Regional Discrimination between NTS Explosions and Western U.S. Earthquakes*, Bull. Seismol. Soc. Am. *79*, 1142–1176.

TAYLOR, S. R. (1996), *Analysis of High-frequency Pg/Lg Ratios from NTS Explosions and Western U.S. Earthquakes*, Bull. Seismol. Soc. Am. *86*, 1042–1053.

TAYLOR, S. R., and HARTSE, H. E. (1997), *An Evaluation of Generalized Likelihood Ratio Outlier Detection to Identification of Seismic Events in Western China*, Bull. Seismol. Soc. Am. *87*, 824–831.

TAYLOR, S. R., and HARTSE, H. E. (1998), *A Procedure for Estimation of Source and Propagation Amplitude Corrections for Regional Seismic Discriminants*, J. Geophys. Res. *103*, 2781–2789.

WALTER, W. R., MAYEDA, K. M., and PATTON, H. J. (1995), *Phase and Spectral Ratio Discrimination between NTS Earthquakes and Explosions. Part I: Empirical Observations*, Bull. Seismol. Soc. Am. *85*, 1050–1067.

XIE, J. K., and MITCHELL, B. J. (1990), *A Back-projection Method for Imaging Large-scale Lateral Variations of L_g Coda Q with Application to Continental Africa*, Geophys. J. Int. *100*, 161–181.

ZHANG, T. R., and LAY, T. (1994), *Analysis of Short-period Regional Phase Path Effects Associated with Topography in Eurasia*, Bull. Seismol. Soc. Am. *84*, 119–132.

(Received August 24, 1999, revised February 10, 2000, accepted April 24, 2000)